

Metal Rich Plasma at the Center Portion of the Cygnus Loop

Emi MIYATA*, Hiroshi TSUNEMI*, Takayoshi KOHMURA, and Seiji SUZUKI

Department of Earth and Space Science, Graduate School of Science, Osaka University

1-1, Machikaneyama, Toyonaka, Osaka, 560

E-mail(EM) : miyata@ess.sci.osaka-u.ac.jp

and

Shiomi KUMAGAI

Department of Physics, College of Science and Technology, Nihon University

Kanda-Surugadai 1-8, Chiyoda-ku, Tokyo 101

(Received ; accepted)

Abstract

We observed the center portion of the Cygnus Loop supernova remnant with the ASCA observatory. The X-ray spectrum of the center portion was significantly different from that obtained at the North-East (NE) limb. The emission lines from Si and S were quite strong while those of O and the continuum emission were similar to those obtained at the NE limb. Based on the spectral analysis, Si and S emission lines originated from a high-kTe and low ionization plasma whereas O and most of the continuum emission arose from a low-kTe and high ionization plasma. We suppose that Si and S emitting gas are present

at the interior of the Loop while O lines and continuum emission mainly arise from the shell region. Therefore, we subtracted the spectrum of the NE limb from that of the center. Obtained abundances of Si, S, and Fe were 4 ± 1 , 6 ± 2 , and $1.3_{-0.3}^{+0.6}$ times higher than those of the cosmic abundances, respectively, and are ~ 40 times richer than those obtained at the NE limb. These facts strongly support that some of the crude ejecta must be left at the center portion of the Cygnus Loop. The low abundance of Fe relative to Si and S suggests a type II SN with a massive progenitor star as the origin of the Cygnus Loop.

Key words: Supernovae, supernova remnants — Abundances — X-rays: spectra

1. Introduction

The heavy elements present in the hot gas in galaxies are thought to be supplied both by stellar winds and by supernovae (SNe). Theoretical calculations of the nucleosynthesis of the SNe have been improved greatly in the past ten years (e.g., Thielemann, Nomoto, & Hashimoto 1990; Thielemann, Nomoto, & Hashimoto 1996, hereafter TNH). In contrast, the observational evidences of metal rich gas have been obtained for only a limited number of young supernova remnants (SNRs).

Ku et al. (1984) first performed spatially-resolved spectroscopy on the Cygnus Loop with the Einstein observatory. They constructed an X-ray image with spatial resolution of $\sim 1'$ in the energy region of 0.1–4.0 keV. The X-ray image clearly showed limb-brightening

* CREST, Japan Science and Technology Corporation (JST)

structure. They noticed that $k\text{Te}$ at the limb was generally lower than that at the center. Charles, Kahn, & McKee (1985) found that $k\text{Te}$ gradually increased toward the center from the vicinity of the limb. Tsunemi et al. (1988) observed the whole Cygnus Loop with the Gas Scintillation Proportional Counters on board the Tenma satellite, which possessed roughly twice better energy resolution than that of the proportional counter (Koyama et al. 1984). They detected emission lines from highly ionized Si and S. They fitted the X-ray spectrum in combination with the spectrum obtained with a previous rocket observation (Inoue et al. 1979, 1980). They found that a two-component NEI model could reproduce the X-ray spectra. Together with Charles et al. (1985), Tsunemi et al. (1988) suggested that tenuous high- $k\text{Te}$ plasma was sitting in the interior region which was surrounded by dense low- $k\text{Te}$ plasma. Such high- $k\text{Te}$ component was confirmed by Hatsukade & Tsunemi (1990) with the Ginga satellite.

Due to its high sensitivity, high energy resolution, and wide energy band, the ASCA observatory has opened a new window for the physics of hot plasmas like SNRs. We can perform the plasma diagnostics in detail by using the X-ray CCD cameras. So far, the abundances of heavy elements have been well determined for many young SNRs with the ASCA observatory (see review by Tsunemi & Miyata 1997). For evolved SNRs, it is difficult to determine the abundances due to low- $k\text{Te}$, low surface brightness, and large interstellar absorption. Furthermore, the swept up interstellar medium (ISM) dominates the ejecta mass from the progenitor star. This makes it difficult to detect the ejecta.

The Cygnus Loop is an evolved SNR and one of the best studied SNRs. Since the Cygnus Loop is roughly 8 degrees away from the Galactic plane, the neutral hydrogen column (N_{H}) is only a few $\times 10^{20} \text{ cm}^{-2}$. This enables us to detect emission lines from O

and to determine kTe with high accuracy. The mass of the swept up ISM is estimated to be roughly $100 M_{\odot}$ since the average density of the ISM is 0.2 cm^{-3} and the mean radius is 18.8 pc (Ku et al. 1984). In comparison, the mass of the ejecta ranges from one to several tens M_{\odot} . Thus, the ejecta are submerged under the sea of the ISM. However, due to its high surface brightness and large apparent size, we can perform spatially-resolved analysis for the Cygnus Loop. This enables us to search ejecta in detail if ejecta have not yet mixed well with the ISM.

The first observation of the Cygnus Loop with the ASCA observatory was performed by Miyata et al. (1994; hereafter MTPK) on the NE limb. They found that kTe increased toward the center whereas $\log(\tau)$ decreased. They determined the abundances of heavy elements from O to Fe and found that metals were deficient at the NE limb.

In this *paper*, we present the observational results of the center portion of the Cygnus Loop observed with the ASCA observatory. The X-ray spectrum obtained from the center portion was quite different from that obtained at the NE limb. We studied the plasma diagnostics of the interior of the Cygnus Loop and nucleosynthesis at the SN, apart from dense shell regions.

2. Observations and Results

We observed the center portion of the Cygnus Loop with the ASCA observatory for ~ 15 ks on Apr. 20–21, 1993 during the ASCA performance-verification phase. The ASCA observatory, the fourth Japanese X-ray satellite (Tanaka, Inoue, & Holt 1994), is equipped with four X-ray telescopes (XRT; Serlemitsos et al. 1995) that simultaneously

feed four focal plane instruments. The telescopes have a point spread function (PSF) with a half power diameter of about $3'$. The focal plane detectors are two Solid-state Imaging Spectrometers (SIS; Burke et al. 1991) and two Gas Imaging Spectrometers (GIS; Ohashi et al. 1996; Makishima et al. 1996). The SISs have a FOV of $22' \times 22'$ and an energy resolution of approximately 60 eV full width at half maximum below 1 keV. The GISs have a higher effective area above 3 keV and larger FOV than the SISs. We focused on the SIS data for the spectra analysis and used the GIS data to investigate the spatial variation.

Figure 1 shows the location of our SIS FOV superimposed on the X-ray surface brightness map of the Loop (Aschenbach 1994) with a black square. It is centered at $\alpha = 20^{\text{h}}51^{\text{m}}56^{\text{s}}$ and $\delta = 31^{\text{d}}09'02''$ (2000). The location of the observation by MTPK toward the NE limb is also shown in this figure.

There were several correction factors (Echo, DFE, CTI, and RDD) in the SIS data analysis (Dotani et al. 1995; Dotani et al. 1997). As mentioned in Dotani et al. (1997), the energy resolution of the SIS gets worse due to the RDD effects, particularly for 4 CCD mode data. Our data were obtained just after the launch and the energy degradation caused by the RDD effects could be negligibly small. Thus, we corrected only Echo, DFE and CTI. Since these effects could be corrected only for the Faint mode data, we focused only on the Faint mode data for the spectrum analysis. The observing time of the Faint mode data was ~ 5.6 ks after screening the data. We subtracted blank sky spectra (NEP and Lynx field regions) as the background since we estimated the contribution of the Galactic X-ray background to be negligibly small (Koyama et al. 1986). The count rate in our FOV was $\sim 8.8 \text{ c s}^{-1} \text{ SIS}^{-1}$.

Another serious background component for an extended source is stray light (Serlemitsos et al. 1995). We estimated the contamination of the center portion of the Cygnus Loop caused by the bright shell regions. The count rate of the stray light from the shell regions was roughly 0.2 c s^{-1} , which was only 2 % of the total count rate of the center portion. Therefore, we can safely ignore the contamination from the bright shell regions. See the appendix for more detail.

2.1. *Spectrum Fitting*

The X-ray spectrum of our FOV is shown in figure 2, which was the sum of the data from two SISs. K emission lines of O, Ne, and Mg were relatively weak while those of Si and S, and L emission lines of Fe were quite strong compared with those obtained at the NE limb (MTPK). We detected three emission lines for Si: Si XIII $K\alpha$, $K\beta$, and Si XIV $K\alpha$. Using the line intensity ratios of these emission lines, we can determine the ionization condition of the X-ray emitting plasma as mentioned in section 2.1.2.

2.1.1. *NEI model (Fit I)*

We first applied the NEI model coded by K. Masai (Masai 1984) to our data (hereafter we refer this fitting as Fit I). The NEI model is characterized both with kTe and with $\tau \equiv n_e t$, where n_e is an electron density [cm^{-3}] and t is an elapsed time [s] after the shock heating. In this model, we calculated the evolution of the ionization with a constant kTe . kTe mainly depends on the shape of the continuum emission while τ can be determined either by line intensity ratios of a given element or by the line center energies of He-like ions. The abundances of O, Ne, Mg, Si, S, Fe, and Ni were set to be free parameters.

That of He was set to be a cosmic value (Allen 1973) whereas those of C and N were fixed to that of O. N_{H} was fixed to $4 \times 10^{20} \text{ cm}^{-2}$ (Inoue et al. 1979; Kahn et al. 1980). The best fit curve is shown in figure 2 and derived parameters are summarized in table 1. This model was far from an acceptable fit, with a reduced χ^2 of 18 (degrees of freedom (dof) = 77). From the statistical point of view, a large discrepancy was found around 0.6 keV, where emission lines from O VII and O VIII were present. The best fit model could not reproduce the line intensity ratio between O VII and O VIII. The data requested higher intensity from O VII and lower intensity from O VIII than the model provided. This suggested lower ionization state and/or lower kTe than that expected from the best fit model. The other large discrepancy was found around Fe–L blends in the energy range of 0.8–1.2 keV, where Fe–L emission lines must be dominant. We should note that the best fit model also could not reproduce the line intensity ratios between Si XIII $K\alpha$, $K\beta$, and Si XIV $K\alpha$. The data preferred higher intensity from Si XIII $K\beta$ than that of the best fit model, which suggested higher kTe.

Through the model fitting by using the NEI model, we found that no model with a single component could reproduce the line intensity ratios of O and Si lines simultaneously. This means that a multi-component plasma is present along the line of sight in our FOV. This is natural since Charles et al. (1985) and Sauvageot, Decourchelle, & Tsunemi (1995) found gradients in kTe and MTPK found gradients both in kTe and in $\log(\tau)$ along the radius in the Cygnus Loop. From the theoretical point of view, we can expect such gradients for SNRs in the adiabatic phase (e.g., Itoh 1979) even if we consider the Coulomb heating of electron gas (Shklovskii 1962; Ito 1978). These observational results and theoretical calculations suggest that the value of kTe increases toward the explosion center. Thus,

we suppose that emission lines of Si mainly arise from the inner region while those of O arise from the outer region.

2.1.2. Combination model (Fit II)

Next, we applied a model of thermal bremsstrahlung and Gaussian line profiles, a combination model as noted in MTPK, in order to evaluate the emission lines (hereafter we refer this fitting as Fit II). Free parameters were center energy, line width, normalization of each Gaussian line, kTe and normalization of thermal bremsstrahlung. Applying the F-test with a significance level of 99 % to determine the number of Gaussian lines and continuum emission, we found that 13 Gaussian lines and two components of continuum emission with different kTe significantly improved χ^2 value. The significance level of the last component added (the 2.24 keV line) was ≥ 99 %. No additional component could improve the χ^2 value even at the 90 % confidence level. The best fit curve is shown in figure 3. The best fit parameters for Gaussian line profiles are summarized in table 2. We identified each line and the results are shown in this table. The line width of each Gaussian line profile except Fe-L blends, Si XIII $K\alpha$, and S XV $K\alpha$ is negligibly small, taking into account the energy resolution of the SIS. Obtained kTe values are 0.24 ± 0.01 and $1.1_{-0.5}^{+3}$ keV and the reduced χ^2 is 1.0 with dof of 57. The equivalent width of each emission line is also given in this table.

We found that the continuum emission consisted of two components with different kTe. Such high-kTe component was first detected by the Tenma satellite (Tsunemi et al. 1988) and confirmed by the Ginga satellite (Hatsukade & Tsunemi 1990). Based on their observation of the whole Cygnus Loop, these authors suggested that the tenuous high-kTe

plasma fills the interior region which was surrounded by the dense low-kTe plasma. Due to the projection effect, we can easily imagine that we detected at least two types of plasma with different kTe and different density when we observed at the center portion.

The obtained kTe for the low-kTe component is well within the range obtained at the NE limb (0.23–0.30 keV). The emission measures ($n_e^2 L$ [pc cm⁻⁶]: L is the plasma length along the line of sight [pc]) of the two components were 14 ± 1 and $(5_{-4}^{+16}) \times 10^{-2}$ pc cm⁻⁶ for the low-kTe component and the high-kTe component, respectively. Therefore, we suppose that most of the continuum emission arises from low-kTe and high density shell region.

We calculated the line intensity ratios of Si XIII K α to Si XIII K β and Si XIV K α to Si XIII K α . The former is sensitive to kTe and the latter is sensitive both to kTe and to $\log(\tau)$. Thus, we can determine the plasma condition for Si. Figure 4 shows the confidence contours of these intensity ratios on a $\log(\tau)$ –kTe plane, based on the calculations performed by Masai (1984). The area shaded with right-down lines shows the 90 % confidence area of Si XIII K α / Si XIII K β while that with right-up lines shows the 90 % confidence area of Si XIV K α / Si XIII K α . We can restrict the plasma condition of Si as $kTe \geq 1.5$ keV and $\log(\tau) \leq 10.6$, suggesting significant departure from the collisional ionization equilibrium (CIE) condition. This high kTe value is consistent with that of the continuum emission of the high kTe component. These results suggest that there is a hot unevolved plasma somewhere along the line of sight.

For S emission lines, we could not detect S XV K β or higher ionization ions. Therefore, we could determine neither kTe nor $\log(\tau)$ by using the line intensity ratios. As shown by Tsunemi et al. (1986), the center energies of the lines from the ions of heavy elements

up to He-like depend both on kTe and on $\log(\tau)$. The variation of the line center energy for S is large compared with other elements (O–Si) under the plasma conditions we are concerned with. We calculated the apparent line center energy for S in a $\log(\tau)$ – kTe plane as shown in figure 5. We included lines in the energy range of 2.3 to 2.5 keV from highly ionized ions of S up to He-like ions. The 90 % error region for the apparent line center energy of S is shown by the shaded area. From this figure, we found that the kTe of the S emitting plasma was quite high (≥ 1.5 keV) and similar to that of Si. The ionization timescale can be determined to be ≥ 10.6 . When we considered the systematic errors of 10 eV in the determination of the energy scale, kTe and $\log(\tau)$ for S emitting plasma could be restricted to ≥ 1 keV and ≥ 10.5 , respectively. Therefore, $kTe \simeq 1.5$ keV and $\log(\tau) \simeq 10.6$ is acceptable both for Si and for S.

We next studied the equivalent widths as shown in table 2. We found remarkable large equivalent widths for Si and S lines for which we investigated whether the plasma with the cosmic abundance could account or not. The equivalent width of the emission line depends on kTe , $\log(\tau)$, and the elemental abundance. Figures 6–7 show the equivalent widths of Si and S in a $\log(\tau)$ – kTe plane, assuming the cosmic abundance. We summed all emission lines from Si in the energy range from 1.839 to 1.866 keV to calculate the figure 6. For figure 7, we considered all emission lines from S in the energy range from 2.3 to 2.5 keV. The maximum values of the equivalent width in $kTe \leq 100$ keV are roughly 0.9 keV and 0.5 keV for Si and S, respectively. The kTe range in figure 6 surely covers the kTe range we have to consider. Therefore, the above values can be considered as maximum for our purpose. These maximum values are much smaller than those we obtained. This indicates that the abundances of Si and S are higher than those of cosmic values.

We estimated the most plausible values and lower limits for the abundances of Si and S. As shown in figures 6–7, the equivalent widths of Si and S are ~ 0.6 keV and ~ 0.3 keV for the cosmic plasma with $kTe=1.5$ keV, $\log(\tau)=10.6$. Therefore, we calculated the most plausible abundances by dividing the observed equivalent widths by these values and got 4 and 8 times larger than the cosmic abundances for Si and S, respectively. In the same way, we calculated the lower limits of abundances by dividing observed equivalent widths by the maximum values in the case of cosmic abundances. Obtained lower limits for Si and S were 3 and 5. Therefore, we established the over-abundance for Si and S at the center portion. Adding to the studies of line intensity ratios, we suppose that hot unevolved plasma containing rich Si and S is sitting at the center portion of the Cygnus Loop along the line of sight.

We also calculated the line intensity ratio for O emission lines. The line intensity ratio of O VIII to O VII was 0.47 ± 0.04 . This value was consistent with the average value obtained by MTPK (0.15–0.80). This means that the plasma condition of O at the center portion is similar to that at the NE limb. Next, we compared the line intensities at the center portion with those at the NE limb. Due to the projection effect, if we observe at the center portion, we detect emission both from the shell region and from the interior region. At the shell region, we could expect low- kTe continuum and strong O emission lines as we detected at the NE limb. Since the plasma length at the center was different from that at the NE limb, we compared intensities of O lines by using the equivalent width. At the NE limb, the equivalent widths for O VIII and O VII were 0.17 and 0.20 keV, respectively. In table 2, we calculated equivalent width of each emission line by using both continuum emission components. If we calculated equivalent widths by using the low- kTe component

solely, we obtained 0.18 and 0.20 keV for O VIII and O VII, respectively. These values are in good agreement with those obtained at the NE limb. This fact strongly suggests that all of O emission lines were accounted for by the low-kTe component, which would be present at the shell region. Therefore, we can safely assume that the emission lines of O mainly come from the shell region which is seen at the center portion due to the projection effect.

In summary of Fit II, we obtained high kTe values both for Si and for S based on the studies of ratios of emission line intensities. We confirmed that Si and S emitting gas was over-abundant based on the studies of equivalent widths. On the other hand, most of the continuum emission arose from the low-kTe component and the obtained kTe value was similar to that obtained at the NE limb (MTPK). The line intensity ratio of O VIII to O VII was also consistent with that obtained at the NE limb. These results suggest that Si and S arise from the interior plasma with high-kTe ($\simeq 1.5$ keV) showing significant departure from the CIE condition ($\log(\tau) \simeq 10.6$) while most of the continuum emission and O arise from the low-kTe plasma in the shell region.

2.2. Comparison with the NE Limb

Figure 8 shows the X-ray spectra obtained both at the center portion and at the NE limb. We normalized these spectra by equalizing line intensities of O. The emission lines from Si, S, and Fe in the center portion are much stronger than those in the NE limb, whereas the line intensity ratios of O VIII to O VII are similar, as indicated in section 2.1.2. To evaluate the emission from the interior region (hereafter we refer to this region as the ‘core’ region), we subtracted the spectrum of the NE limb from the center portion

by equalizing the intensity of O lines. Figure 9 shows the limb-subtracted spectrum.

Si, S, and Fe–L blends were prominent in the core spectrum. We again applied the NEI model to this spectrum (hereafter we refer this fitting as Fit III). The abundance of He was fixed to the cosmic value. Since those of C, N, and O could not be determined, we fixed them to 0.25 which was obtained in the Fit I. Free parameters were kTe , $\log(\tau)$, emission measure, abundances of Ne, Mg, Si, S, Fe, and Ni. The best fit curve is shown in figure 9 and the best fit parameters are summarized in table 1. Whereas fits were significantly improved, this model was not yet acceptable from the statistical point of view (reduced χ^2 of 2.8 with dof of 71). Large discrepancy could be found again at the energy region of Fe–L (~ 1.2 keV). Liedahl, Osterheld, & Goldstein (1995) recalculated emissivities of Fe–L lines and found deviations from the previously known model, especially for the atomic code of Fe XXIII–Fe XXIV ($3 \rightarrow 2$). The NEI model we currently used should still be tuned up to take account of the new atomic code. However, except for the 1.2 keV energy region, other Fe–L lines (≤ 1 keV) were well reproduced with the current model, and the abundance of Fe must be determined with these lines from the statistical point of view. Therefore, we expect that abundance of Fe would be reliable.

The obtained kTe was consistent with that of the continuum emission for the high- kTe component in Fit II but was slightly lower than that obtained from the studies of line intensity ratios of Si. We should note that we obtained higher kTe (1.1 ± 0.3) if we fitted the core spectrum with the same model in the energy range of 1.5–4 keV. In this case, the obtained abundances were consistent with those obtained with Fit III because the statistical errors became large.

Obtained abundances of Si and S were much larger than those of the cosmic abundances.

The abundance of Fe was consistent with the cosmic value. These values were roughly 40 times larger than those obtained at the NE limb (MTPK). These results indicate that hot and low ionization condition plasma with rich Si, S, and Fe is present along the line of sight at the center portion of the Cygnus Loop.

3. Discussion

3.1. Concentration of Heavy Elements at the Core Region

We applied the NEI model to the core spectrum and obtained an over-abundance for Si, S, and Fe. Compared to the abundances obtained at the NE limb (MTPK), those obtained at the core region were a factor of ~ 40 larger. The plasma condition of the Si and S emitting plasma is in high- kT_e and in low ionization state, suggesting its presence at the interior region of the Cygnus Loop. These facts strongly support that the X-ray emitting plasma at the core region is the ejecta in origin. Chevalier (1974) and Mansfield & Salpeter (1974) suggested that some amount of mass of a progenitor star would remain at the core region of the remnant even in an evolved SNR like the Cygnus Loop. Our results also indicate that the mixing of ejecta into the ISM did not occur effectively.

We then investigated the extent of the Si, S, and Fe emitting region. Fe emission lines are in the energy region of 0.7–1.3 keV where we expect many emission lines from other elements. On the contrary, in the energy region of 1.8–2.5 keV, we expect only Si and S emission lines. Since MTPK found the deficient abundance of Fe at the NE limb, we suppose that emission lines from Fe would arise from the similar region to those of Si and S. We extracted the GIS image with the narrow energy range of 1.8–2.5 keV where

GIS possesses large effective area. Emission in this energy band arose from a circular region with a radius of $\sim 9' \approx 2$ pc as shown in figure 10. Assuming a spherical uniformly emitting region (filling factor was set to unity), we calculated the density and mass of heavy elements listed in table 3.

3.2. Comparison with Theoretical Calculations

We compared the derived abundances of Si, S, and Fe with those predicted by the theoretical calculations of nucleosynthesis in the SNe. After the explosive processing of heavy elements by the passing of the supernova shock, heavy elements are formed in a so-called “onion-skin” structure. Light elements like C, N, or O are sitting in outer layers whereas heavier elements like Si, S, or Fe are produced at the inner region (TNH). It is not reasonable to compare our results with the mean abundance of nucleosynthesis for an entire star (table 3 in TNH), since we observed only the core region of the Cygnus Loop. Therefore, we integrated the abundances of the heavy elements from an explosion center ($M_r = M_0$; M_r is mass radius and normalized by the stellar mass) toward some mass radius ($M_r = M_1$), considering the mass fraction diagrams as shown in figure 7 in Nomoto, Thielemann & Yokoi (1984) for type Ia (W7 model) and figure 1 in TNH for type II with various progenitor star masses. For the type Ia model, M_0 is zero while for the type II model, M_0 is fixed to the mass cut radius described in table 4 in TNH. The neutron star or black hole would form inside the mass cut. We summed up ^{56}Ni , ^{57}Ni , and Fe to calculate the Fe mass. Figure 11 shows the comparison of the derived mass ratios of S/Si and Fe/Si (shown by dotted lines) with the model calculations of the type Ia model (a) and type II models with progenitor masses of $15M_\odot$ (b), $20M_\odot$ (c), and $25M_\odot$ (d). In

general, if we integrate from M_0 to some mass radius, we can trace along the solid lines from upper right to lower left in each diagram.

The type Ia model predicts the mass of Fe to be much larger than that of Si and could not reproduce our results even if we set M_1 to be $1.4M_\odot$.

For the type II model, TNH cannot precisely determine the location of the mass cut, with the result that the Fe abundance is rather uncertain. The Fe mass predicted by the type II model with $20M_\odot$ was well determined based on the observation of SN1987A. Since the radioactive decays of $^{56}\text{Ni} \rightarrow ^{56}\text{Co} \rightarrow ^{56}\text{Fe}$ power the light curve, the amount of ^{56}Ni was determined to be $0.075M_\odot$ (e.g., Arnett et al. 1989). In the same way, the Fe mass in the type II model with $15M_\odot$ was also confirmed since the derived Fe mass based on the light curve of 1993J was $0.1M_\odot$ (e.g., Nomoto et al. 1993).

The type II model with progenitor mass less than $20M_\odot$ can reproduce the mass ratio of S to Si we obtained. However, the total mass of Fe is much larger than that of Si even if we integrate from the mass cut radius to the outermost layer. Therefore, the observed mass ratio of Fe to Si cannot be explained with these models.

For the type II model with $25M_\odot$, we can explain the obtained mass ratio of S to Si as well as Fe to Si with a reasonable value of M_1 ($2.0\text{--}3.9M_\odot$). When we integrate from $M_0 = 1.77M_\odot$ to $M_1 = 2.0M_\odot$, the predicted masses of Si, S, and Fe are 0.063 , 0.035 , and $0.041M_\odot$. Therefore, we can explain the derived masses of Si, S, and Fe with the $25M_\odot$ model if roughly 1 % of the ejecta sitting at $1.77M_\odot \leq M_r \leq 2.0M_\odot$ is still present at the core region of the Cygnus Loop. We also estimated the acceptable range of M_0 . We found $1.77 \leq M_0 \leq 1.85$ can reproduce the mass ratios we obtained. This result suggests that the mass inside $1.77\text{--}1.85M_\odot$ will collapse into a neutron star.

Our results support the model proposed by McCray & Snow (1979). McKee & Cowie (1975) suggested that there would exist dense clouds in the vicinity of the Cygnus Loop in order to explain the differences in the shock velocities seen at optical wavelengths (Minkowski 1958) and in the soft X-ray region (Gorenstein et al. 1971). McCray & Snow (1979) proposed that such dense clouds would be associated with the formation of a stellar wind bubble by an early-type progenitor star, meaning type II SN origin of the Cygnus Loop. Charles et al. (1985) also suggested type II origin based on the inhomogeneities in the X-ray image. It should be noted that we were the first to determine the stellar type of the progenitor of the Cygnus Loop supernova based on the elemental abundance ratios of the ejecta as determined from X-ray lines.

The most ejecta have left our FOV. Considering the metal deficiency at the NE limb, we suppose that most ejecta, including all light elements like O or Mg as well as Si, S, and Fe, are still inside the shell and isolated from the ISM. If it is the case, the contact discontinuity, which separates the ejecta from the shocked ISM, may be seen as the abundance discontinuity.

A SN explosion with a progenitor mass of $\geq 10M_{\odot}$ is thought to form a neutron star. We expect that a neutron star with a mass of $1.77-M_{\odot}$ should have born at the SN explosion that created the Cygnus Loop. So far, there is no observational evidence of a neutron star associated with the Cygnus Loop. Further deep observations in the radio and X-ray wavelengths are strongly encouraged to confirm the massive star origin of the Cygnus Loop.

4. Conclusion

We observed the center portion of the Cygnus Loop supernova remnant with the X-ray CCD cameras on board the ASCA observatory. We confirmed a significant departure from a collisional ionization equilibrium condition at the center portion. Obtained abundances at the core region were larger than those of cosmic abundances for Si, S. Moreover, abundances of Si, S, and Fe were ~ 40 times larger than those obtained at the NE limb. This strongly supports the hypothesis that the X-ray emitting plasma in the core is ejecta in origin. Although previous X-ray observations could not detect any signature of ejecta, we could find it by using both the imaging capability and the high energy resolving power of the ASCA observatory.

Obtained abundances can be compared with theoretical calculations of nucleosynthesis by a SN explosion. Since we only observed the core region, we integrated the model calculations from the explosion center to some mass radius. For the explosion models for type Ia SN or for type II with the progenitor mass less than $20 M_{\odot}$, the abundance of Fe is much larger than that of Si or S even if we integrate to the outermost radius. On the other hand, the abundances of Si, S, and Fe can be explained with the type II model with $25 M_{\odot}$ if we integrate these abundances from the mass cut radius $1.77 M_{\odot}$ to $2 \sim 3.9 M_{\odot}$. Therefore, our results suggest the massive progenitor origin of the Cygnus Loop and the existence of the stellar remnant associated with the Cygnus Loop.

We would like to acknowledge Prof. Nomoto and Drs. T. Suzuki and K. Iwamoto for fruitful discussions about the theoretical aspects of the SNRs at conference of Thermonuclear Supernovae. Dr. B. Aschenbach kindly gave us the whole X-ray image of the Cygnus

Loop obtained with the ROSAT all-sky survey. We thank Dr. Thielemann to use his data on nucleosynthesis of SNe. We would like to thank the anonymous referee for her or his detailed comments and suggestions which greatly improved this paper.

We are grateful to all the members of ASCA team for their contributions to the fabrication of the apparatus, the operation of ASCA, and the data acquisition. We thank the members of ASCA_ANL/Sim ASCA software team.

Appendix. Effects of stray light

We estimated the effects of stray light. For the ASCA X-ray telescope, XRT, some X-rays coming from an off axis angle of $0.5\text{--}1.5^\circ$ can reach the focal plane (Serlemitsos et al. 1995). There are mainly four kinds of stray paths expected: 1) single reflection by primary mirrors (referred as Primary); 2) single reflection by secondary mirrors (Secondary); 3) direct (No-reflection); and 4) a few times reflections by front and back surfaces of mirrors (Abnormal) (Tsusaka et al. 1994). There are no bright X-ray stars around the Cygnus Loop. However, if we observe the center portion of the Loop, the contamination by emission from the bright shell region might be important.

We simulated stray light effects in the frame work of ASCA_ANL/Sim ASCA ver. 0.9. We used the code of the ray tracing, XRTraytr ver 2.1 developed by the XRT team (and modified by us). This code simulated the average performance of the four XRTs and did not consider the characteristics of each telescope.

We assumed limb-brightening features with the inner and outer radii of $72'$ and $84'$, which were similar to the global structure of the Cygnus Loop as shown in figure 1. We

also estimated the stray light as well as the usual double reflections (Normal) when we observed the center portion of the Cygnus Loop. Under this configuration, we confirmed no X-rays from the bright shell region of the Cygnus Loop reached the focal plane as Normal.

Figure 12 shows the results of our simulations for the SIS. The coordinate system is DETX/Y which is a detector coordinate system. The horizontal and vertical gaps are due to the physical spaces between the CCD chips of the SIS. We rebinned each image by 4×4 pixels. We generated 7 million 1 keV photons for each stray component. The fraction of each component was written below each figure. In total, 0.1 % of the incident photons came into the whole FOV of the SIS as stray light shown in the right-lower. We should note that the relative intensity of the stray light increases toward the edge of the detector.

We did not yet obtain the whole image of the Cygnus Loop with the ASCA observatory. The whole image of the Cygnus Loop obtained with the ROSAT all-sky survey showed the inhomogeneities of the shell regions (Aschenbach 1994). We, here, estimated the contamination for the worst case. We assumed the count rate of the shell region per each $22'$ square to be the same as that of the NE limb and 13 s^{-1} which was one of the brightest regions in the ROSAT energy band and also the brightest region in the ASCA energy band ever observed. Thus, the total count rate of the shell region could be estimated as roughly 170 s^{-1} , resulting in the contamination to the center portion of 0.17 s^{-1} . This count rate was similar to that of the background including both the internal background and the CXB (Gendreau et al. 1995). This value was only 2 % of the total count of the center portion and we concluded that we could safely ignore the contamination from the bright shell regions.

References

- Allen, C.W. 1973, *Astrophysical Quantities* 3rd ed. (The Athlone Press), p.30
- Arnett, W.D., Bahcall, J.N., Kirshner, R.P., Woosley, S.E. 1989, *ARA&A*, 27, 629
- Aschenbach, B. 1994, *New Horizon of X-ray Astronomy*, eds. F. Makino & T. Ohashi (Universal Academy Press inc.), p.103
- Burke, B.E., Mountain, R.W., Daniels, P.J., Cooper, M.J., & Dolat, V.S. 1991, *IEEE Trans.*, ED-38, 1069
- Charles, P.A., Kahn, S. M., & McKee, C. F. 1985, *ApJ*, 295, 456
- Chevalier, R.A. 1974, *ApJ*, 188, 501
- Cox, D.P. 1972, *ApJ*, 178, 169
- Dotani, T., Yamashita, A., Rasmussen, A., & the SIS team, 1995, *ASCA News Letter* 3, p.25
- Dotani, T., Yamashita, A., Ezuka, H., Takahashi, K., Crew, G., Mukai, K., & the SIS team, 1997, *ASCA News Letter* 5, p.14
- Gendreau, K.C. Mushotzky, R., Fabian, A.C., Holt, S.S., Kii, T., Serlemitsos, P.J., Ogasaka, Y., Tanaka, Y. et al. 1995, *PASJ*, 47, L5
- Gorenstein, P., Harris, B., Gursky, H., & Giacconi, R. 1971, *Science*, 172, 369
- Hatsukade, I., & Tsunemi, H. 1990, *ApJ*, 362, 566
- Inoue, H., Koyama, K., Matsuoka, M., Ohashi, T., Tanaka, Y., & Tsunemi, H. 1979, *X-Ray Astronomy*, eds. W.A. Baity & L.E. Peterson (Pergamon Press, Oxford), p.309
- Inoue, H., Koyama, K., Matsuoka, M., Ohashi, T., Tanaka, T., & Tsunemi, H. 1980, *ApJ*, 238, 886

- Itoh, H. 1978, PASJ, 30, 489; Erratum, 31, 429
- Itoh, H. 1979, PASJ, 31, 541
- Kahn, S.M., Charles, P.A., Bowyer, S., & Blissett, R.J. 1980, ApJ, 242, L19
- Koyama, K., Ikegami, T., Inoue, H., Kawai, N., Makishima, K., Matsuoka, M. Mitsuda, K., Murakami, T. et al. 1984, PASJ, 36, 659
- Koyama, K., Makishima, K., Tanaka, Y., & Tsunemi, H. 1986, PASJ, 38, 121
- Ku, W.H.-M., Kahn, S.M., Pisarski, R., & Long, K.S. 1984, ApJ, 278, 615
- Liedahl, D.A., Osterheld, A.L., & Goldstein, W.H. 1995, ApJ, 438, L115
- Makishima, K., Tashiro, M., Ebisawa, K., Ezawa, H., Fukazawa, Y., Gunji, S., Hirayama, M., Idesawa, E. 1996, PASJ, 48, 171
- Mansfield, V.N., & Salpeter, E.E. 1974, ApJ, 190, 305
- Masai, K. 1984, Ap&SS, 98, 367
- McCray, R., & Snow, T.P. 1979, ARA&A, 17, 213
- McKee, C.F., & Cowie, L.L. 1975, ApJ, 195, 715
- Minkowski, R. 1958, Rev.Mod.Phys. 30, 1048
- Miyata, E., Tsunemi, H., Pisarski, R., & Kissel, S. E. 1994, PASJ, 46, L101 (MTPK)
- Nomoto, K., Thielemann, F.-K., & Yokoi, K. 1984, ApJ, 286, 644
- Ohashi, T., Ebisawa, K., Fukazawa, Y., Hiyoshi, K., Horii, M., Ikebe, Y., Ikeda, H., Inoue, H. et al. 1996, PASJ, 48, 157
- Sauvageot, J.L., Decourchelle, A., & Tsunemi, H. 1995, UV and X-ray Spectroscopy of Astrophysical and Laboratory Plasmas, eds. K. Yamashita & T. Watanabe (Universal Academy Press inc.), p.303
- Serlemitsos, P.J., Jalota, L., Soong, Y., Kunieda, H., Tawara, Y., Tsusaka, Y., Suzuki,

- H., Sakima, Y. et al. 1995, PASJ, 47, 105
- Shklovskii, I.S. 1962, Sov.Astron., 6, 162
- Tanaka, Y., Inoue, H., & Holt, S.S. 1994, PASJ, 46, L37
- Thielemann, F.-K., Nomoto, K., & Hashimoto, M. 1990, Supernovae, Les Houches, Session LIV, eds. S.Bludman, R.Mochkovitch & J.Zinn-Justin, p.629
- Thielemann, F.-K., Nomoto, K., & Hashimoto, M. 1996, ApJ, 460, 408 (TNH)
- Tsunemi, H., Yamashita, K., Masai, K., Hayakawa, S., & Koyama, K. 1986, ApJ, 306, 248
- Tsunemi, H., Manabe, M., Yamashita, K., & Koyama, K. 1988, PASJ, 40, 449
- Tsunemi, H., & Miyata, E. 1997, Thermonuclear Supernovae, eds. P.Ruiz-Lapuente, R. Canal, & J. Isern (Kluwer Academic Publishers), p.561
- Tsusaka, Y., Suzuki, H., Awaki, H., Yamashita, K., Kunieda, H., Tawara, Y., Ogasaka, Y., Uchibori, Y. et al. 1994, SPIE, 2011, 517

Fig. 1. The X-ray surface brightness map of the Cygnus Loop obtained with the ROSAT all-sky survey (Aschenbach 1994). The black squares show the FOV of the center portion and the NE limb (MTPK) as observed with the ASCA observatory.

Fig. 2. X-ray spectrum of the center portion of the Cygnus Loop. Upper pannel shows the data points with $\pm 1 \sigma$ errors and the best fit curve with the NEI model (Fit I). Lower pannel shows the residuals of the fit in the unit of σ .

Fig. 3. Same as figure 2, but for the combination model (Fit II).

Fig. 4. The line intensity ratios of three Si lines in a $\log(\tau)$ -kTe plane. The area shaded with right-down lines shows the 90 % confidence area of Si XIII $K\alpha / K\beta$ while that with right-up lines shows the 90 % confidence area of Si XIV $K\alpha / \text{Si XIII } K\alpha$.

Fig. 5. Center energy of the apparent S plotted in a $\log(\tau)$ -kTe plane. We considered the highly ionized ions up to He-like ions. The shaded area shows the 90 % confidence area for the line center energy of S.

Fig. 6. The contour map of the equivalent widths [keV] of Si in a $\log(\tau)$ -kTe plane

Fig. 7. Same as figure 6, but for S.

Fig. 8. Spectrum of the center portion. For comparison, the spectrum obtained at the NE limb is also shown by equalizing at O line intensities.

Fig. 9. The spectrum of the core region of the Cygnus Loop. The solid line shows the best fit curve of the NEI model (Fit III).

Fig. 10. Narrow-band (1.8–2.5 keV) image obtained with the GIS. The FOV of the GIS is shown by solid circle.

Fig. 11. Comparison of the derived mass ratios (S/Si and Fe/Si) with model calculations for nucleosynthesis of type Ia (a) and type II with $15M_{\odot}$ (b), $20M_{\odot}$ (c), and $25M_{\odot}$ (d) progenitor mass. In the model calculations, we integrated abundances of Si, S, and Fe from M_0 to M_1 and calculated S/Si and Fe/Si for each M_1 . Several M_1 values are shown in diagrams in M_{\odot} unit. Dotted lines show the regions we obtained in 90 % confidence level.

Fig. 12. Simulated images of the stray light for No-reflect, Primary, Secondary, and Abnormal. The right-lower image is the sum for all components. The vertical and horizontal gaps are due to the physical spaces between the CCD chips.

Table 1. Fitting results of the Masai model applied to the X-ray spectra extracted from the center portion and the core region

Parameter	Whole spectrum	Core spectrum
	Fit I	Fit III
kTe [keV]	0.51 ± 0.01	$0.82^{+0.09}_{-0.07}$
$\log(\tau)$	10.54 ± 0.03	$10.35^{+0.06}_{-0.07}$
Emission Measure [pc cm^{-6}] ^a	0.71 ± 0.06	0.10 ± 0.03
Abundance [relative to cosmic values]		
C,N,O	0.25 ± 0.02	0.25 (fixed)
Ne	0.46 ± 0.04	$0.2^{+0.2}_{-0.1}$
Mg	$0.34^{+0.05}_{-0.04}$	$0.3^{+0.3}_{-0.2}$
Si	$1.9^{+0.2}_{-0.1}$	4 ± 1
S	5.4 ± 0.6	6 ± 2
Fe	0.46 ± 0.04	$1.3^{+0.6}_{-0.3}$
Ni	7 ± 1	5^{+3}_{-2}
reduced χ^2 (dof)	18 (77)	2.8 (71)

NOTED – Quoted errors are at 90% confidence level.

^a Emission measure in unit of $\text{pc}^3 \text{cm}^{-6}$ was directly obtained from the spectrum analysis.

We converted it to emission measure in unit of pc cm^{-6} to divide the obtained value by $22' \times 22'$ ($\simeq 24 \text{pc}^2$).

Table 2. The Observation Line Features (Fit II)

Observed energy [keV]	Flux [10^{-3} photons $s^{-1}cm^{-2}$]	Ion species identified	Equivalent width [keV]
0.573 ± 0.002	40 ± 2	O VII	0.19
0.659 ± 0.003	19 ± 1	O VIII	0.14
0.726 ± 0.003	14 ± 1	Fe XVII	0.09
0.822 ± 0.003	35 ± 1	Fe XVII	0.69
0.928 ± 0.003	6.0 ± 0.4	Ne IX, Fe XVIII, Fe XIX	0.11
1.018 ± 0.004	2.9 ± 0.2	Ne IX, Ne X, Fe XVII, Ni XX	0.12
1.121 ± 0.007	3.1 ± 0.2	Fe XVII	0.29
1.251 ± 0.008	0.57 ± 0.09	Fe XIX, Ni XIX	0.09
1.353 ± 0.005	0.54 ± 0.06	Mg XI	0.15
1.872 ± 0.002	1.02 ± 0.05	Si XIII	2.3
2.07 ± 0.03	0.04 ± 0.02	Si XIV	0.16
2.24 ± 0.01	0.12 ± 0.02	Si XIII	0.81
2.463 ± 0.008	0.21 ± 0.03	S XV	2.3

NOTED – Systematic errors (about 10eV) are not included.

– Quoted errors are at 90% confidence level.

Table 3. Densities and masses of heavy elements at the core region

Elements	Density [10^{-5}cm^{-3}]	Mass [$10^{-4}M_{\odot}$]
Si	4 ± 1	5_{-1}^{+2}
S	$2.7_{-0.8}^{+1.1}$	4 ± 1
Fe	$1.4_{-0.4}^{+0.6}$	$2.9_{-0.8}^{+1.4}$

NOTED – Quoted errors are at 90% confidence level.

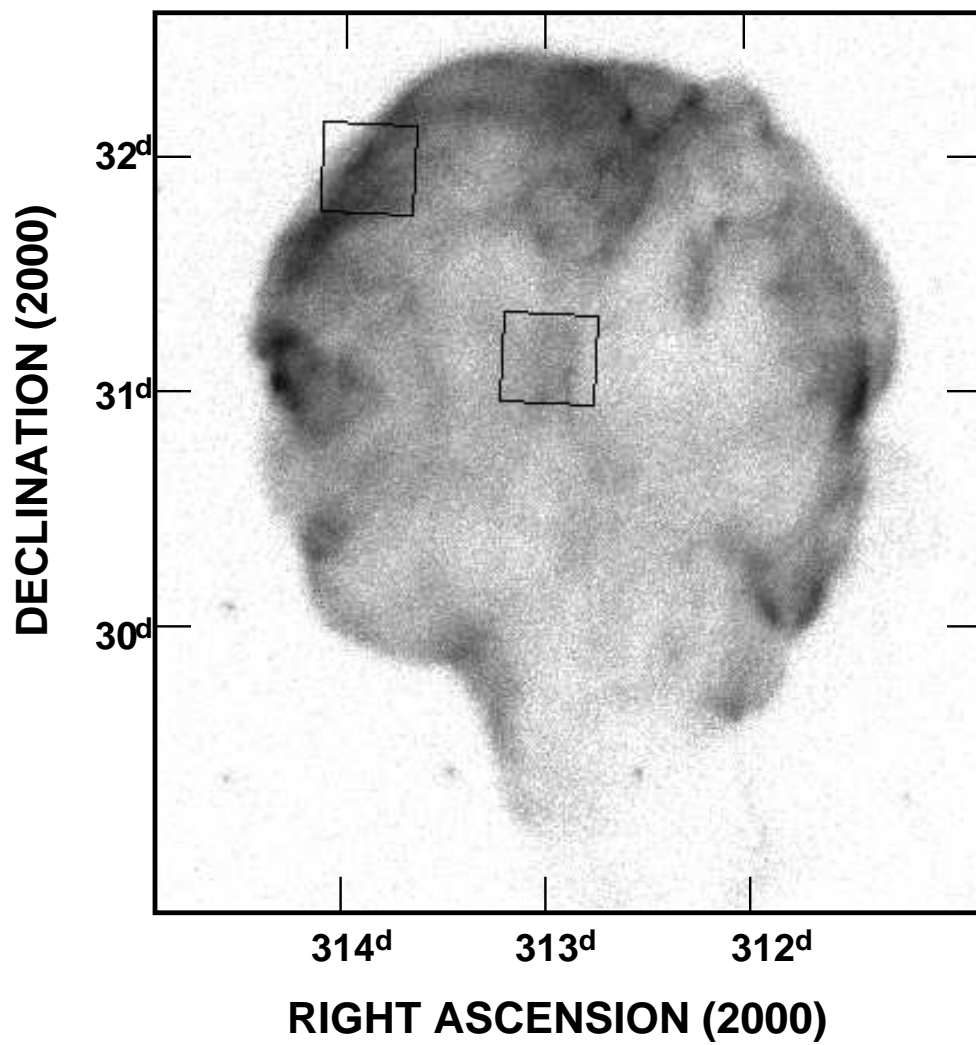


Fig. 1..

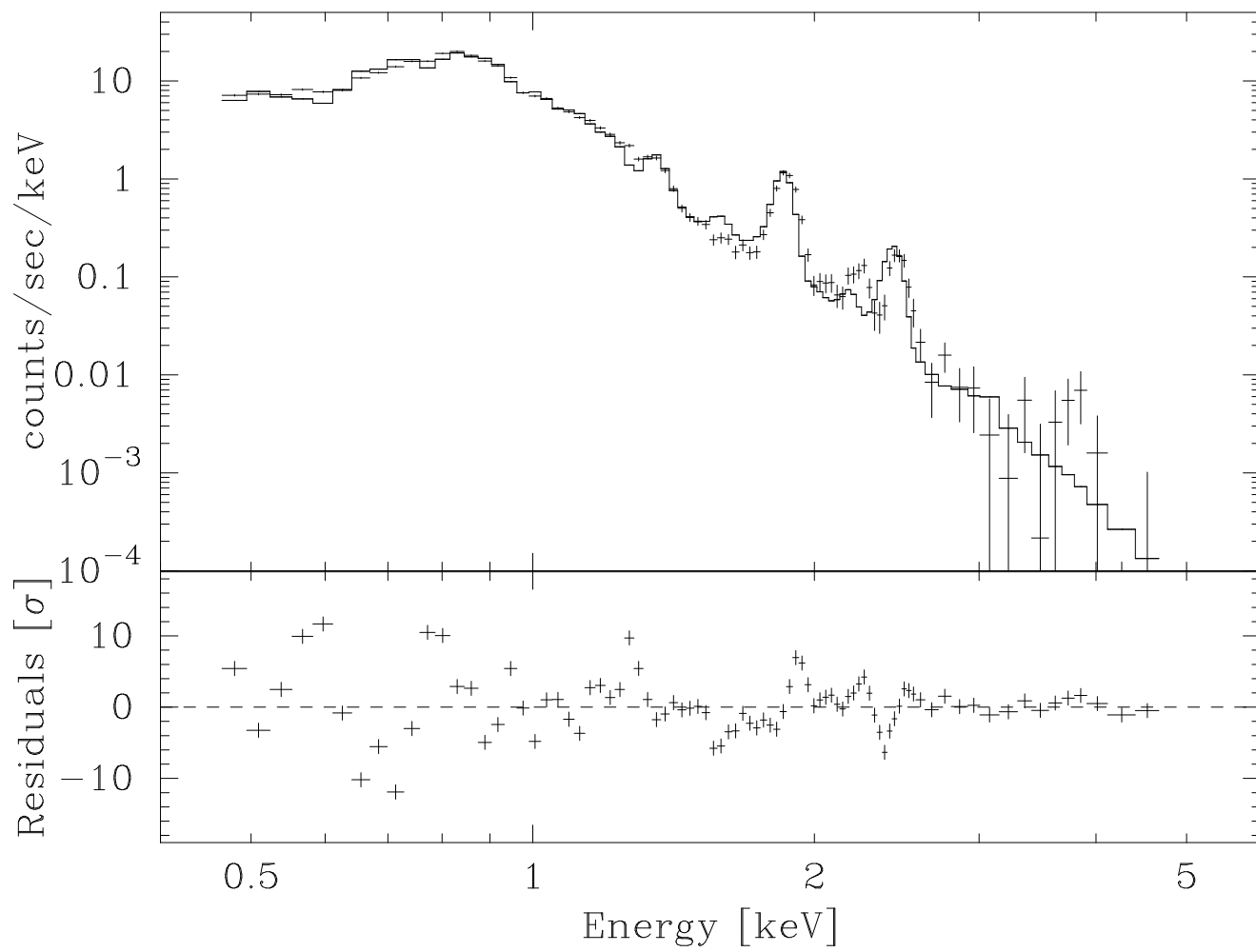


Fig. 2..

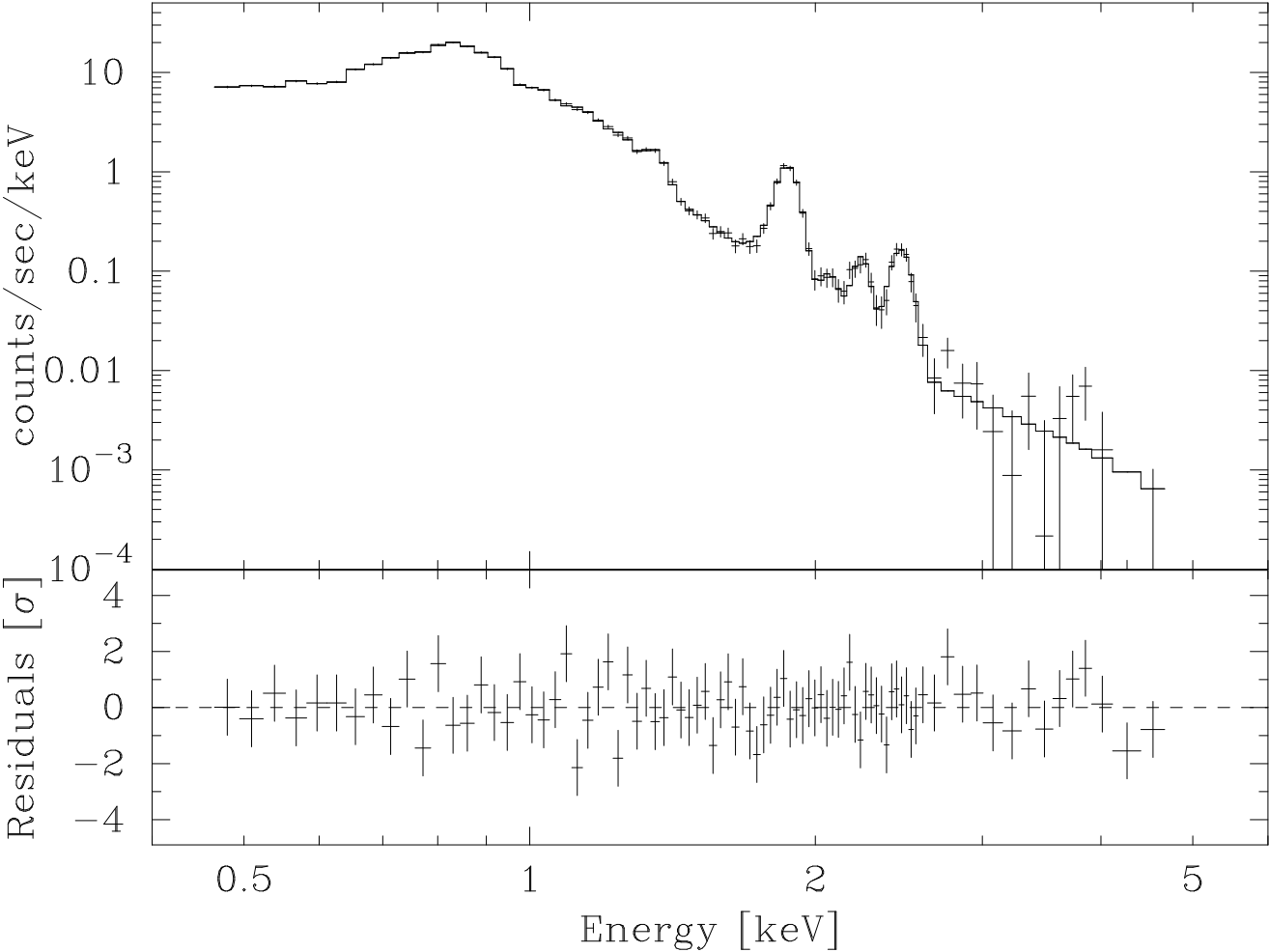


Fig. 3..

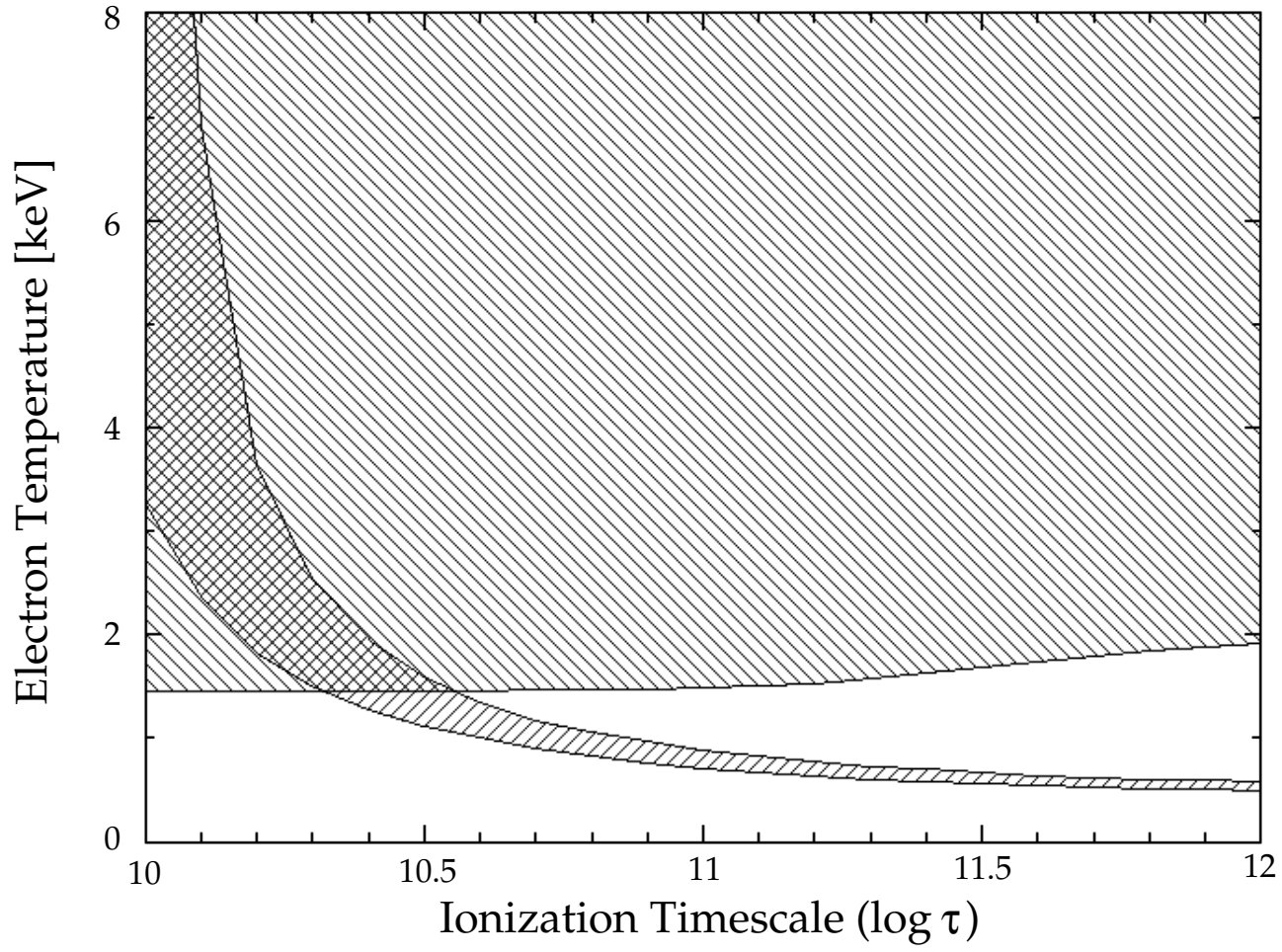


Fig. 4..

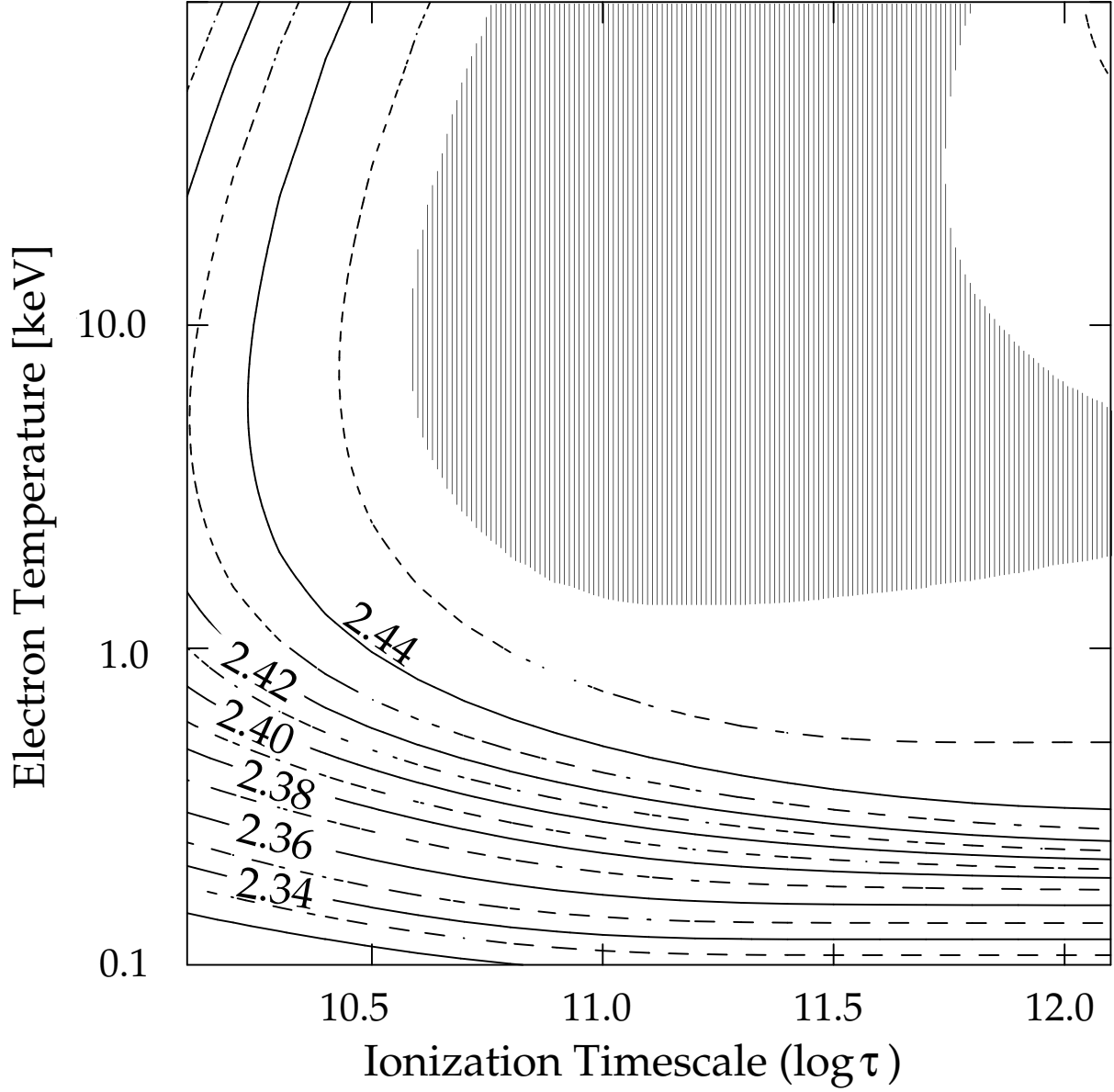


Fig. 5..

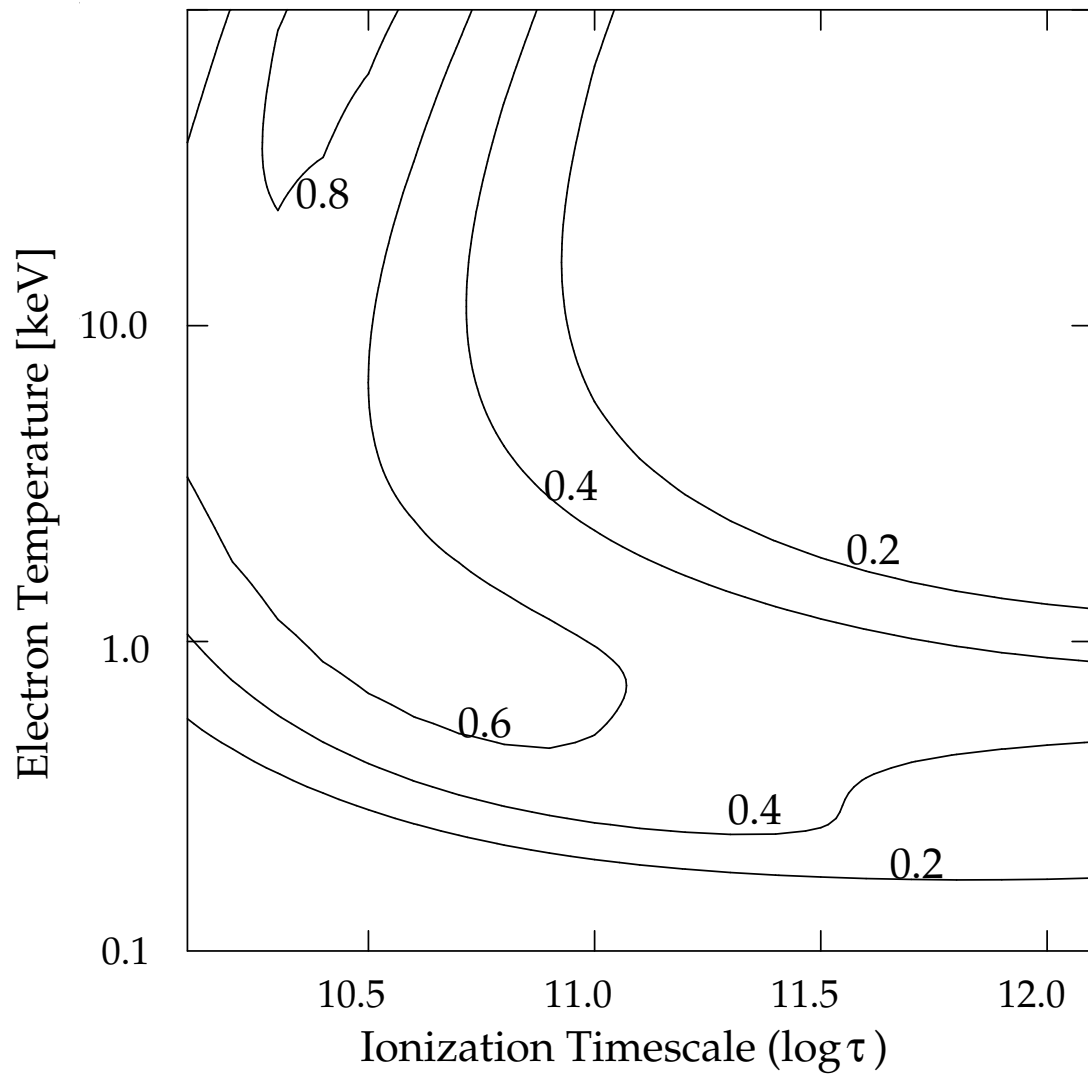


Fig. 6..

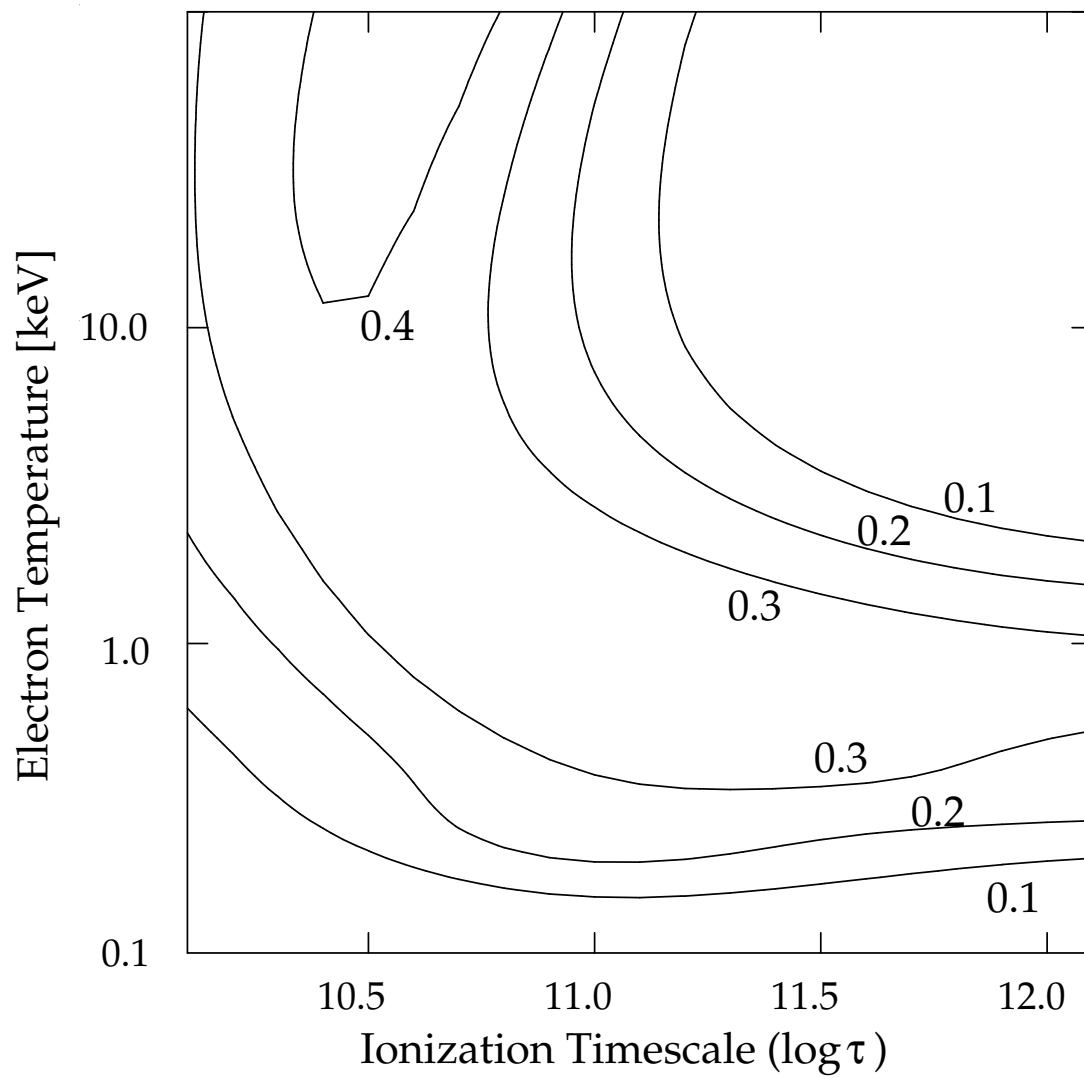


Fig. 7..

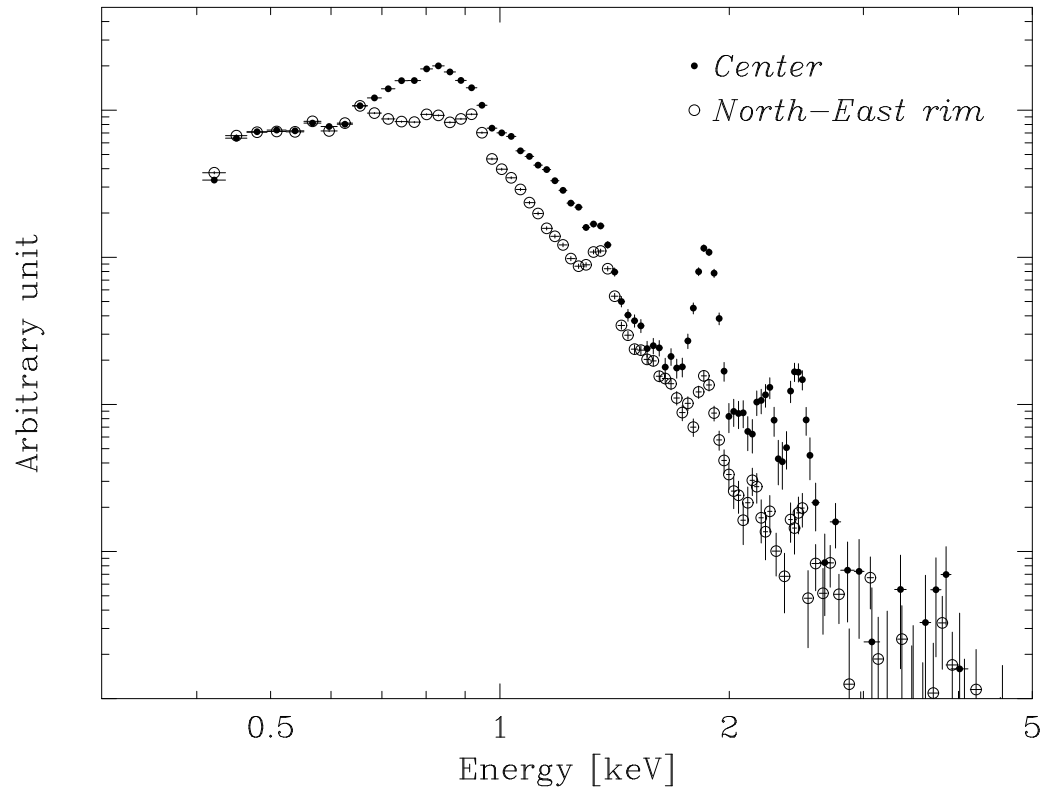


Fig. 8..

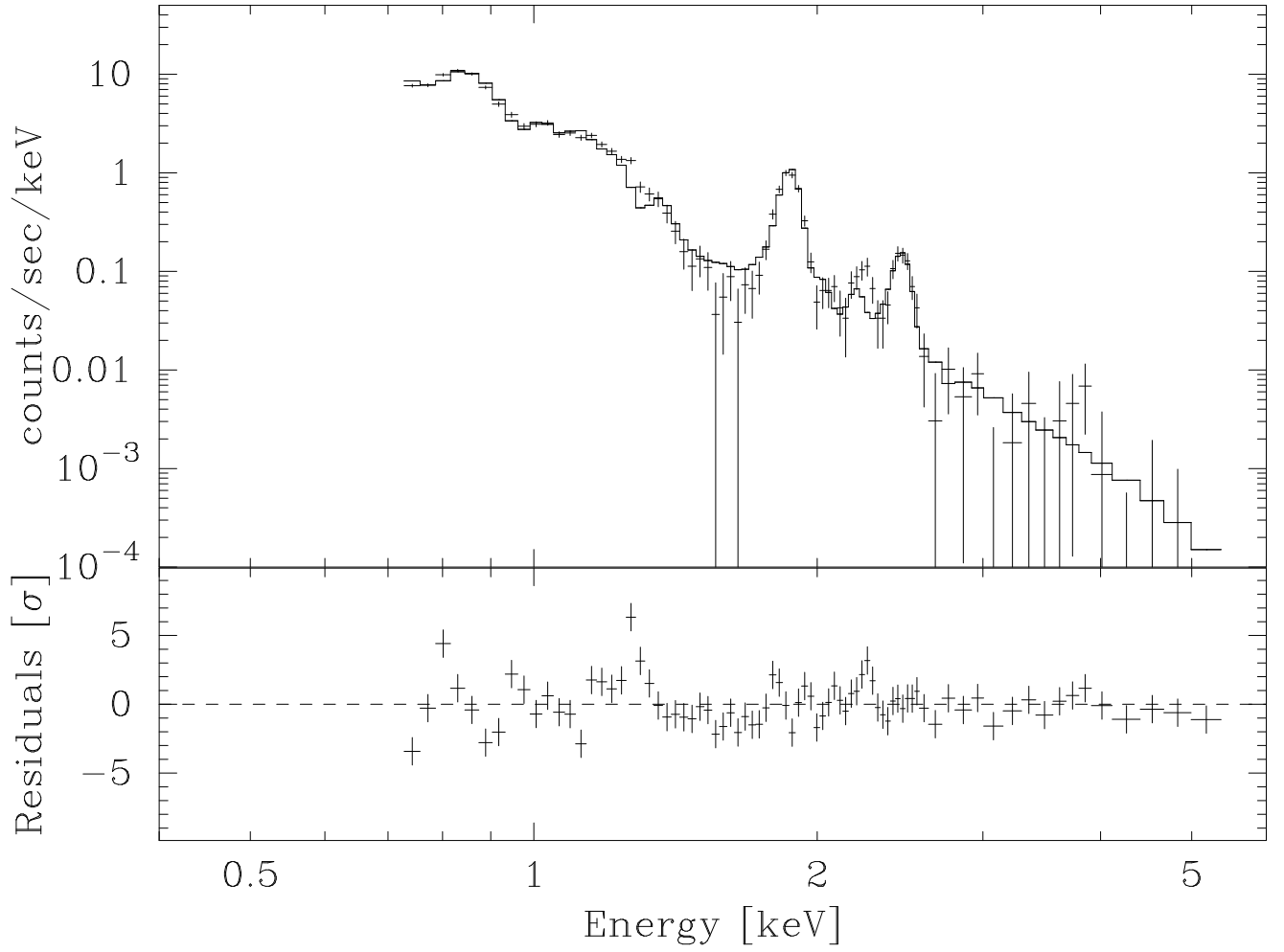


Fig. 9..

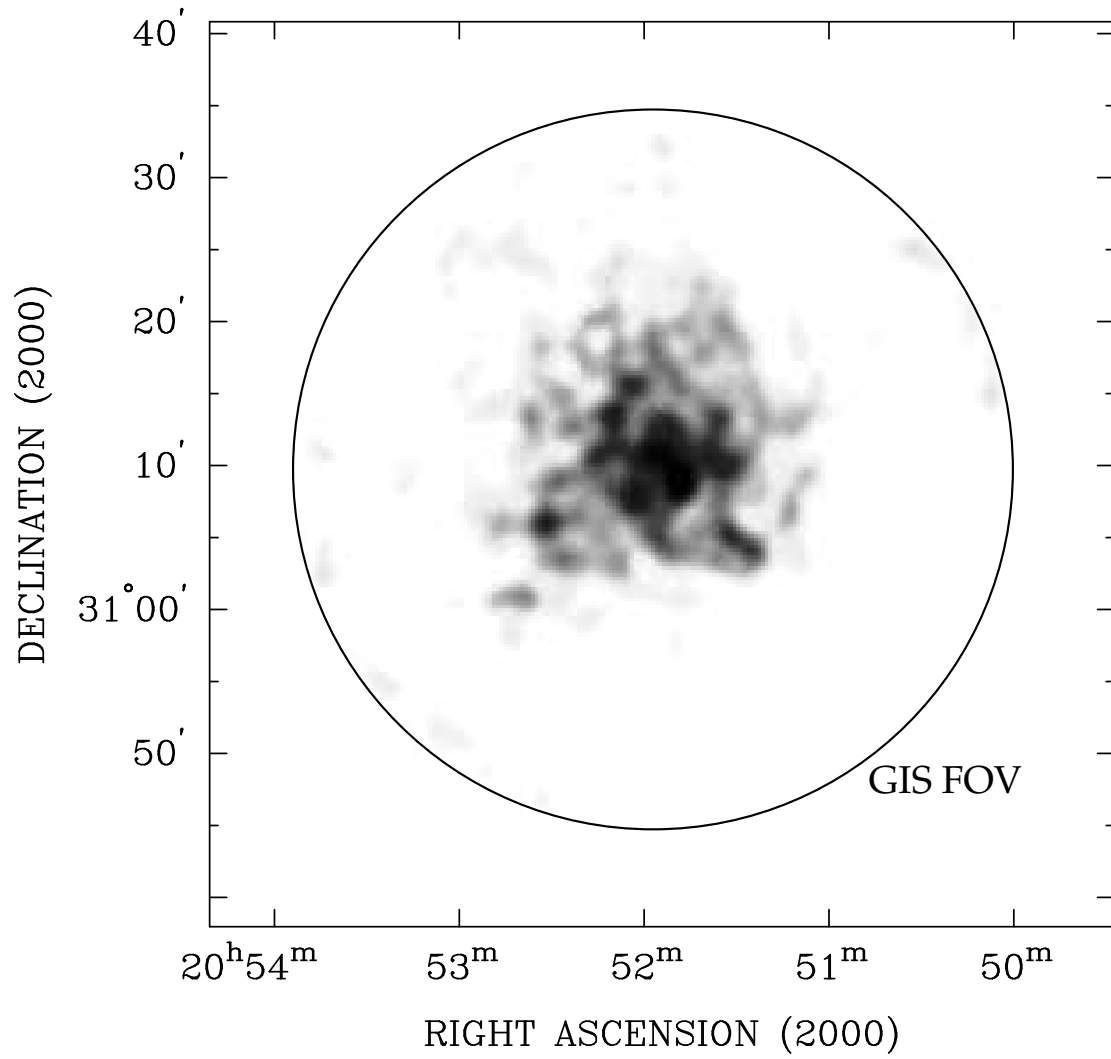


Fig. 10..

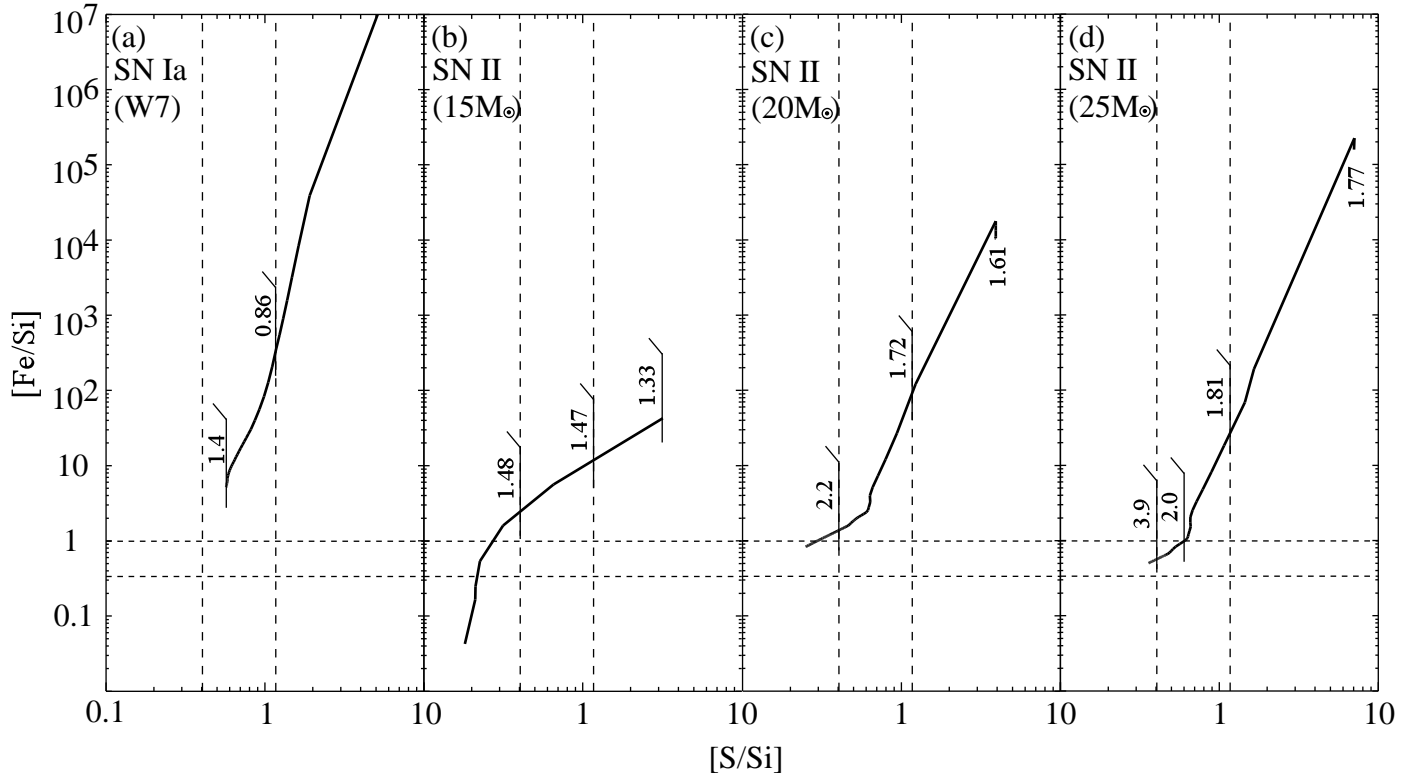


Fig. 11..

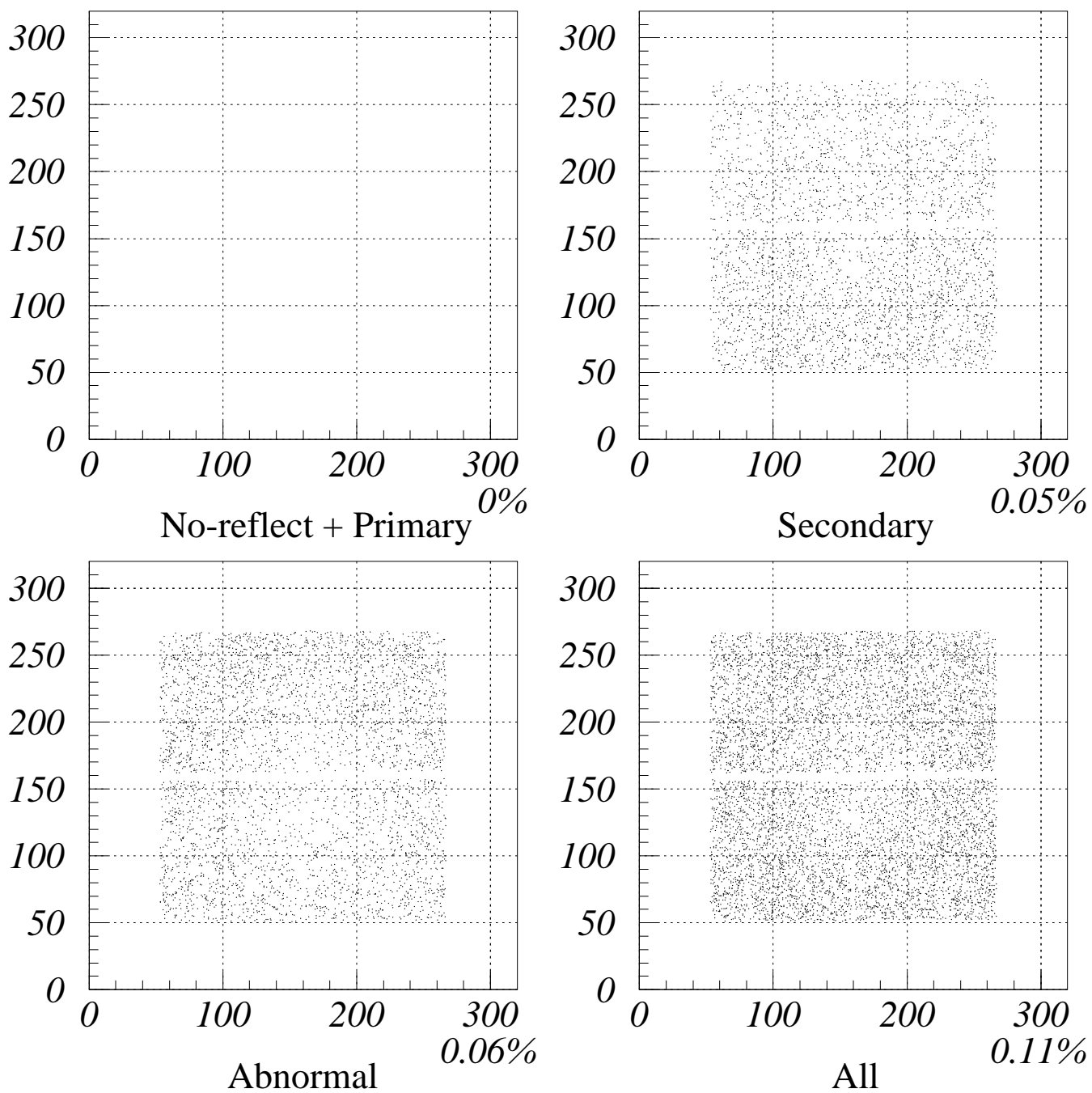


Fig. 12..